Polymer Stiffness Governs Template Mediated Self-Assembly of Liposome-Like Nanoparticles: Simulation, Theory and Experiment

Journal:	*Nanoscale*
Manuscript ID	NR-ART-08-2019-007063.R1
Article Type:	Paper
Date Submitted by the Author:	30-Sep-2019
Complete List of Authors:	Shen, Zhiqiang; University of Connecticut, Mechanical Engineering Loe, David ; University of Connecticut, Department of Chemistry Fisher, Alessandro; University of Connecticut, Mechanical Engineering Kroger, Martin; ETH Zurich, Polymer Physics Rouge, Jessica; University of Connecticut, Department of Chemistry Li, Ying; University of Connecticut System, Mechanical Engineering

Polymer Stiffness Governs Template Mediated Self-Assembly of Liposome-Like Nanoparticles: Simulation, Theory and Experiment

Zhiqiang Shen ‡, a, *David T. Loe* ‡, b, *Alessandro Fisher* a, *Martin Kröger* c, *Jessica L. Rouge**, b, *and Ying Li**, a, d

a Department of Mechanical Engineering, University of Connecticut, Storrs, CT 06269, USA

b Department of Chemistry, University of Connecticut, Storrs, CT 06269, USA

c Department of Materials, Polymer Physics, ETH Zürich, CH-8093 Zurich, Switzerland

d Polymer Program, Institute of Materials Science, University of Connecticut, Storrs, CT 06269, USA

‡ These authors contributed equally.
* Corresponding author: Ying Li, E-mail: yingli@engr.uconn.edu; Jessica L. Rouge, Email: jessica.rouge@uconn.edu.

ABSTRACT:

This study suggests that the self-assembly of a template-mediated liposome (TML) can be utilized as a general method to produce liposomes with controlled sizes. A polymer tethered core is used here as a starting configuration of a TML. Lipids anchored on the free ends of the tethered polymers direct the self-assembly of surrounding free lipid molecules to form liposome-like nanoparticles. Characterizing the flexibility of polymers by their persistence lengths, we performed large scale molecular simulations to investigate the self-assembly process of TMLs with tethered polymers of different stiffness values. The stiffness of tethered polymer is found to play a crucial role in the self-assembly process of TMLs. The flexible and rigid-like polymers can accelerate and delay the self-assembly of TMLs, respectively. In addition, the critical grafting of tethered polymers and required lipid concentration to from perfectly encapsulated TMLs are found to increase with the flexibility of tethered polymers. To scrutinize these simulation-based findings, we synthesized DNA-polyethylene glycol (PEG) TMLs and performed corresponding experiments. To this end we incorporate increasing concentrations of DNA as a proxy for increasing the rigidity of the tethered polymers. We find that the resulting structures are indeed consistent with the simulated ones. Finally, a theory is developed that allows to estimate the required free lipid number (or lipid concentration) and grafting density analytically for polymers of given persistence length. Through these combined computational, experimental, and theoretical studies, we present a predictive model for determining the effect of polymer stiffness on the self-assembly of TMLs, which can be used as a general approach for obtaining perfectly encapsulated TMLs as potential drug delivery vehicles.

Keywords: polymer stiffness, self-assembly, liposome-like nanoparticle, drug delivery, molecular simulation

1. INTRODUCTION

Nanoparticle (NP) mediated drug delivery has attracted great attention due to its promising capability to protect loaded drug molecules and deliver them to diseased cells [1-6]. During the delivery process, NPs need to traverse cellular compartments that present physical barriers to successful drug delivery. For example, proteins in the blood quickly adsorb onto NP surfaces forming often unwanted protein corona effects [7]. These adsorbed proteins can trigger macrophage cells to clear the NPs before they can reach their intended target [8,9]. Therefore, it is crucial that the properties of NPs, such as size, shape, stiffness and surface functionalization, are carefully designed in a predictable manner so that the trajectories of NPs can be better controlled during the cellular delivery and uptake process [10-12]. Although hundreds of different NP formulations have been proposed and synthesized in laboratories, few of them have been transferred successfully to clinical trials due to difficulties in administration that result in a lack of targeted delivery or toxicity *in vivo* [13,14]. Among the various NP candidates designed, liposomes and liposome-like NPs stand out due to their phospholipid composition which can favorably integrate with existing cellular lipid bilayers [15-17]. The phospholipid surface of a liposome resembles the lipid membrane of the cell, often using a lipid composition that contains the same phospholipids that the cell produces, reducing toxicity and immunogenicity as compared to other nanoparticle formulations [18-20]. For instance, by loading doxorubicin into a polyethylene glycol protected liposome, Doxil® became the first U.S. Food and Drug Administration (FDA) approved drug delivery platform [21].

Despite the promising applications of liposomes in drug delivery, it is still challenging to synthesize liposomes with controlled size, geometry and surface chemistry. For instance, to produce liposomes with uniform size distribution, external forces such as sonication and extrusion are necessary for obtaining monodisperse liposomes [22-24]. However, limitations in

experimental set-up, including the duration of the treatment and the position of the ultrasound source and power input, can lead to difficulty in size control during sonication [24]. In addition, liposomes modified through extrusion are limited to the order of several hundred nanometers and to certain lipid compositions [25-27]. Moreover, different lipid compositions can significantly affect the size of a self-assembled liposome. Even when the expected size contribution of a particular lipid used for synthesizing a liposome is known, experimental conditions for synthesizing a specific liposome size and shape remain to be empirically determined [28,29]. This current challenge for experimentalists, to control the liposome size distribution with nanometer precision, is a highly desirable aspect that can contribute greatly to successful drug delivery. It has been shown that the size of various nanomaterials can influence important delivery features such as NP penetration in the extracellular collagen matrix [30,31] and the extent of cellular uptake of NPs during the endocytosis process [32-34]. Therefore, predictable size and reproducible synthesis of liposomes would aid tremendously in the broader application of liposomes for drug delivery and accelerate their clinical applications.

To address these challenges, researchers have begun to explore template-mediated self-assembly of liposomes. For instance, Lin and co-workers utilized a DNA ring as a template for synthesizing highly monodispersed sub-100-nm liposomes with different lipid compositions [35]. The liposome self-assembly process was nucleated and confined inside these rigid DNA nanotemplates with pre-defined sizes. In our recent work, we proposed to use a polymer-tethered inorganic core as a template to guide the self-assembly of liposome-like NPs by taking advantage of highly monodispersed inorganic NPs [36]. As shown in **Figure 1**, our system consists of polymers tethered to an inorganic NP core. These polymers were functionalized with a phospholipid moiety, anchoring individual lipids to the NP core. These anchored lipids act as an initiator, seeding the assembly of free lipids and forming a lipid

bilayer at the surface. We refer to these templated NPs as Core-Polyethylene Glycol-Lipid-Shell Nanoparticles (CPLS NPs), as we use hydrophilic and biocompatible polyethylene glycol (PEG) as the tethered polymer for displaying anchored lipids on the NP surface. Using this new construct, we successfully encapsulated a hydrophilic dye within the PEG layer that is present in the immobilized layer of the CPLS bilayer as a way to indirectly show the presence of a successfully formed lipid bilayer at the nanoparticle's surface. We have predicted that this template-mediated, self-assembled liposome would have inherent advantages over a traditional liposome [36-38]. Specifically, we have shown that we could tune the PEG polymerization degree and core size of the CPLS NP to control its size with high accuracy. We have also demonstrated that our CPLS NPs would have a higher overall stability than a standard liposome when subjected to shear flow [37]. Additionally, the inorganic core can be made of gold, or superparamagnetic iron oxide, to be visible via magnetic resonance imaging for computer tomography for diagnosis purposes, making CPLS NPs a promising multi-functional drug delivery platform.

Using our newly developed CPLS NP system, we have set out to investigate the effects of incorporating different tethered polymers on the template mediated liposome (TML) process inherent to the CPLS NP design. In particular, we have chosen to incorporate tethered DNA molecules, inspired by the spherical nucleic acid (SNA) design [39-41]. SNAs have achieved great success in applications such as gene regulation due to their unique surface properties, including limited toxicity [42], high binding efficiency, enhanced nuclease resistance [43], and minimal immune response [44]. However, further development of SNAs is needed to improve their blood circulation time and bypass their degradation in late endosomes [45-47]. Encapsulating an SNA in a lipid bilayer may reduce the protein absorption and increase its blood circulation time. Additionally, the lipid membrane surface may enable fusion between NPs and cell membranes allowing direct delivery of oligonucleotides into the cytosol [48].

Compared with the flexible nature of PEG polymers, DNA ligands are quite rigid. In simulations they are treated as a rigid rods at the SNA surface [49,50], due to their large persistence length of about 40 nm [51]. Therefore, to understand how the DNA might behave when used as an anchoring unit in the CPLS NP, we chose to investigate what effect adding increasing concentrations of DNA to the current CPLS NP platform would have on the self-assembly process. In this way, we could study the influence of tethered polymer semiflexibility on self-assembly of TMLs, while also providing a strategy for incorporating biodegradable tethers that can dually serve as therapeutic agents within the CPLS NP platform such as antisense oligonucleotides (ASOs) [6].

To test whether the self-assembly of TMLs can serve as a general method to produce liposome-like NPs with different tethered polymers of well controlled size, we systematically investigated the role that polymer stiffness plays in the self-assembly of a TML. A general set of design principles for generating "perfect" TMLs both in respect to polymer stiffness and grafting density are provided through large scale molecular simulations. Furthermore, the incorporation of DNA molecules as a tethered polymer for our new liposome design is explored to help us understand the self-assembly process and the role of the anchoring polymers stiffness as it is related to the extent of liposome bilayer formation. For this purpose, we have experimentally synthesized CPLS NPs consisting of PEG polymers mixed with varying ratios of poly thymidine (polyT) DNA:PEG to mimic the conditions of different persistence lengths within the tethered polymer layer of CPLS NPs. These particles were dually studied via electron microscopy and dynamic light scattering in parallel with dissipative particle dynamic simulations.

The structure of this paper is summarized as follows: First, by investigating the self-assembly process of TMLs through our simulation studies, we found that the stiffness of the tethered polymer greatly influences the self-assembly kinetics of the outer lipid layer (Section 2.1).

Next, we systematically investigated the effect of free lipid number and grafting density on the self-assembly process of TMLs constructed with tethered polymers of four different persistent lengths, and a phase diagram was obtained for each case (Section 2.2). To verify the relevance of these predictions, we synthesized DNA-PEG CPLS NPs in which we incorporated increasing concentrations of DNA as a proxy for increasing the rigidity of the tethered polymer layer of the CPLS NPs. Using dynamic light scattering (DLS) and transmission electron microscopy (TEM) we analyzed the self-assembly process of free lipids on DNA-PEG CPLS NPs upon varying DNA to PEG ratios. We show that the resulting structures present degrees of encapsulation by free lipids that are consistent with the simulated studies, particularly the phase diagrams. Additional details on physical properties available from simulation, such as size and density distributions are examined in Section 2.3. Subsequently, a theory is provided for predicting the size of the TMLs and corresponding optimal conditions for synthesis, indicating ideal grafting densities for the tethered polymer layer and optimal free lipid numbers (Section 2.4). Conclusions are provided in Section 3, followed by details on computational (Section 4.1) and experimental (Section 4.2) methods.

2. RESULTS AND DISCUSSION

2.1. Dynamic process for self-assembly of TMLs

We start our work by investigating the influence of polymer stiffness on the self-assembly process of TMLs in simulations. As given in **Figure 1**, four different polymers with normalized persistence lengths, $\overline{l_p} = 0.17, 0.21, 1.21,$ and 2.21, were assessed, where $\overline{l_p} = l_p/L_0$ is defined as the ratio between the persistence length l_p and polymer counter length L_0. When $\overline{l_p} = 0.17$, the polymer l_p is only 17 percent of its counter length L_0, which indicates a flexible polymer. While for $\overline{l_p} = 2.21$, the polymer l_p is more than twice of its counter length L_0, suggesting an almost rigid rod-like polymer. The radius of the inorganic core in all simulations is fixed as 5 nm. All polymer chains tethered on the inorganic core have the same

6

polymerization degree of $N=30$. To accelerate the self-assembly process, the simulation temperature is controlled at $T=2.0$ (reduced LJ unit). At the beginning of the self-assembly process, the fully relaxed polymer tethered cores are placed in the center of simulation box of $60 \times 60 \times 60$ nm^3, with randomly distributed free lipids. For implementation details see Section 4.1.

Polymer stiffness determines the self-assembly process of TMLs. The snapshots in **Figure 2 (A)** and **(B)** show the evolution of configurations during the self-assembly process of TMLs with polymer grafting density $\sigma_g = 0.35/\text{nm}^2$. Their normalized polymer persistence lengths are $\overline{l_p} = 0.17$ (flexible polymer) and $\overline{l_p} = 2.21$ (rigid rod-like polymer). The free lipid numbers (N_f) for these two cases are kept the same with $N_f = 3500$. As given in **Figure 2 (A)** for $\overline{l_p} = 0.17$, at the beginning of simulation (time $t = 0$), the anchored lipids on terminals of tethered polymers aggregate into several small micelles on the surface of inorganic core. These small micelles act as active sites to recruit the surrounding free lipids due to the strong hydrophobicity of lipid tails in aqueous solution. At $t = 6$ μs, a portion of free lipids are absorbed onto the polymer tethered core due to the anchored lipids. Another portion of free lipids quickly assemble into small micelles due to their amphiphilic nature. Those free micelles continue to fuse with each other, forming free vesicles evolving into a bilayer structure at $t = 224$ μs. More importantly, a portion of free micelles can fuse with the anchored lipid micelles, resulting in vesicles anchored to the inorganic core, which are relatively isolated. The simulation shows that under thermal fluctuations, the free vesicles perform random walks and adsorb by the polymer-tethered core once they fuse with the anchored vesicles. These localized events increase the surface area of the anchored vesicles until they are no longer isolated and are able to make contact and fuse with each other to form a curved bilayer patch that partially covers the core surface ($t = 280$ μs). With the continued adsorption of free vesicles and lipids, the anchored vesicles and bilayer patch increase their

overall size and finally fuse with each other to form a perfect bilayer shell that covers the entire polymer tethered core ($t = 672$ μs). At the end of the simulation, with the direction of anchored lipids, the self-assembly of free lipids results in a perfectly encapsulated TML. Compared with the flexible tethered polymers ($\overline{l_p} = 0.17$), the self-assembled process of TML with rigid rod-like polymers ($\overline{l_p} = 2.21$) exhibits completely different behaviors, as given in **Figure 2 (B)**. At $t = 0$, the lipids displayed at the terminals of tethered polymers also aggregate into separate anchored micelles. At the same time, the polymers form several distinct bundles. Compared to the flexible case in **Figure 2 (A)**, the tethered polymers become straight due to their enhanced stiffness. These rigid polymer bundles also result in a increased distance between the anchored micelles and the inorganic core surface. Over the course of the simulation, the free lipids in the simulation box get absorbed onto the anchored micelles, resulting in the formation of anchored bilayer patch or vesicle ($t = 112, 280$ μs). However, different from those formed from $\overline{l_p} = 0.17$, these anchored lipid structures are far away from each other due to the reduced polymer flexibility. Therefore, they never have the chance to contact and fuse together. Instead, these anchored vesicles and bilayer patches remain isolated, which eventually results in a partially encapsulated TML ($t = 260$ μs). It is important to note that increasing the free lipid number does not qualitatively change the outcome (see **Figure S1** for the case with $N_f = 8500$ in Supporting Information). From these results, we can conclude that the stiffness of tethered polymers influences the self-assembly process and state of TMLs.

High grafting density benefits perfectly encapsulated TMLs. The aforementioned two cases demonstrate that it is more difficult to form a perfectly encapsulated TMLs from tethered polymers with higher stiffness. With this in mind, the next question we sought to answer is how to make a perfectly encapsulated lipid bilayer around an inorganic core when the stiffness of tethered polymers is high. To answer this question, we first investigated the

self-assembly process of rigid rod-like polymers tethered on NPs with high grafting density through simulations, followed by a series of complementary experiments. As shown in **Figure 2 (C)**, while the normalized persistence length of tethered polymers is still $\overline{l_p} = 2.21$. We increased the grafting density to $\sigma_g = 0.8/\text{nm}^2$. The free lipid number in the simulation box is $N_f = 8500$. As we can see in **Figure 2 (C)**, at $t = 0$, the anchored lipids also aggregate to form separated micelles at the terminals of tethered polymers. Compared with the low grafting density scenario in **Figure 2 (B)**, the number of anchored micelles has increased. At $t = 23$ μs, the anchored micelles transform into small bilayer patches as the adsorption of surrounding free lipids occurs. These anchored bilayer patches are able to fuse with each other as they are relatively close to each other, resulting in several curved bilayer patches on the terminals of tethered polymers ($t = 56$ μs). With the further adsorption of free lipids, these curved bilayer patches connect with each other through fusion, forming two large curved patches ($t = 112$ μs). At the end of the simulation, all free lipids are adsorbed onto the surface of the polymer tethered core, resulting in a perfectly encapsulated TML at $t = 764$ μs. Therefore, it can be concluded that increasing the grafting density of tethered polymers benefits the formation of perfectly encapsulated TMLs.

2.2. Phase diagram for self-assembly of TMLs

Both the polymer stiffness and grafting density can greatly affect the self-assembly of TMLs. To quantitatively capture the effects of these parameters, we systematically investigated the self-assembly process of TMLs with four normalized persistence lengths of $\overline{l_p} = 0.17, 0.21, 1.21, 2.21$ characterizing the tethered polymers. Additionally, different grafting densities, ranging from $\sigma_g = 0.05/\text{nm}^2$ to $\sigma_g = 0.8/\text{nm}^2$, were investigated for all four persistence lengths. This resulted in a phase diagram describing the self-assembly states of TMLs as a function of grafting density σ_g and free lipid number N_f at each persistence length. For each point in the phase diagram, two different processes are studied: (1) a polymer

tethered core experiencing a self-assembly process at a specific free lipid number at the temperature of $T = 2.0$; (2) to obtain the self-assembled state at standard temperature (i.e. room temperature), the entire system is annealed to the temperature of $T = 1.0$ within a period of 112 µs after all the free lipids are absorbed on the surface of the polymer tethered inorganic core.

Three different states are discovered for self-assembly of TMLs. As given in **Figure 3**, three qualitatively different self-assembled states can be found in each phase diagram. (1) When the grafting density is below a critical value or the free lipid number is smaller than a critical value, a partially encapsulated state is assembled at the end of the self-assembly process. The partially encapsulated state is mainly due to two reasons: (I) if the grafting density is insufficiently large, anchored vesicles on the terminals of tethered polymers are unable to fuse with each other, resulting in isolated anchored vesicles; (II) if the grafting density is suitable, but the free lipid number still too small, the fused bilayer patches are not large enough to cover the entire surface of the inorganic core. (2) When the grafting density is suitable, but the free lipid number is too large, the anchored lipids form a spherical bilayer with a bud connecting on the surface. This leads to an over-encapsulated state. (3) A perfectly encapsulated state is obtained when both the grafting density and free lipid number fall into a suitable region. By comparing these four phase diagrams, it becomes clear that when synthesizing a perfectly encapsulated TML, the critical grafting density and upper and lower boundaries of free lipid numbers are determined by the degree of polymer semiflexibility.

Critical grafting density of tethered polymers. It is shown in **Figure 3** that the critical grafting density σ_{crit} increases with increasing polymer stiffness. As given in **Figure 3 (A)**, at a persistence length of $\overline{l_p} = 0.17$, the σ_{crit} is located within $(0.05 - 0.2)/\text{nm}^2$. As the persistence length increases to $\overline{l_p} = 0.21$, its σ_{crit} also grows to the range of $(0.2 - 0.35)/\text{nm}^2$. For larger persistence lengths of $\overline{l_p} = 1.21$ and $\overline{l_p} = 2.21$, the σ_{crit} is within $(0.35 -$

0.5)/nm^2. As aforementioned, during the self-assembly process of TMLs, the grafting density is directly proportional to the number of anchored lipids, which form the anchored micelles and direct the whole self-assembly process. This indicates that the grafting density directly determines the probability that the anchored vesicles will fuse with each other and form the anchored curved bilayer patch. Detailed analysis about the relationship between the critical grafting density and polymer stiffness will be discussed in the following section.

Free lipid number boundary. When the grafting density of tethered polymers is larger than the critical grafting density σ_{crit}, the perfectly encapsulated TMLs can only be formed in a limited range of free lipid numbers, defined by the upper and lower free lipid number boundaries. For the normalized persistence lengths of $\overline{l_p} = 0.17$ and 0.21, similar free lipid number boundaries are observed due to their similar persistence lengths. The lower free lipid boundary for different grafting densities falls within 3000-4500. The upper free lipid boundary is located within 4500-6500. Compared to the boundaries of high flexibility polymers, both the lower and upper free lipid boundaries for a persistence length of $\overline{l_p} = 1.21$ increase dramatically. At $\overline{l_p} = 1.21$, the lower boundary is around 5500-7000. Additionally, its upper free lipid boundary is located within 8500-9500. When the persistence length of tethered polymer is further increased to $\overline{l_p} = 2.21$, their free lipid number boundaries shift to larger values again. More importantly, compared to the flexible polymers of $\overline{l_p} = 0.17$ and $\overline{l_p} = 0.21$, the free lipid number boundaries for perfectly encapsulated TMLs become wider for $\overline{l_p} = 1.21$ and $\overline{l_p} = 2.21$.

Experimental validation. In order to see how effectively our simulations reflect the solution-based self-assembly of a TML with a variable grafting density and persistence length, we synthesized four CPLS NPs consisting of two different polymer components, cf. Methods section 4.2. The first polymer is a thiolated heterobifunctional PEG functionalized with a phospholipid, 1,2-distearyl-sn-glycero-3-phosphoethanolamine, (SH-PEG-DSPE) and the

second is a short DNA oligomer, poly thymidine (polyT) used as a backfill. These polymers were mixed in solution prior to adsorption onto the inorganic nanoparticle surface, in this case a 30 nm gold nanoparticle (Au NP), to achieve polymer tethered cores which presented 100%, 75%, 50%, and 0% PEG as seen in **Figure 4**. This method is a slightly modified approach to the synthesis of CPLS NPs that we previously developed (**Figure S2**) [35]. PolyT is a rigid molecule approximately 7 nm in length. We chose a thymidine homo polymer of DNA as it is least likely to have hydrogen bonding with itself and is known to pack well on Au NP surfaces [52]. Through the incorporation of the rigid thiolated polyT DNA at the surface of the CPLS NP in increasing concentrations relative to the SH-PEG-DSPE, we sought to limit the conformational flexibility and the grafting density of the tethered PEG-DSPE to determine the effects this rigid backfill would have on the extent of templated encapsulation possible on the polymer tethered core. As can be seen in **Figure 4**, with increasing amounts of polyT incorporated at the NP core's surface, the ability of the free lipid to fully encapsulate the core is diminished. The distribution of various states of lipid encapsulation, defined as perfectly encapsulated, budding (over encapsulation), anchored vesicles, and no encapsulation was observed and tallied as a function of total number of particles analyzed (200 CPLS particles per sample) to determine relative encapsulation distributions of each state (see Supporting Information Section 3 for counting protocol). Additional TEM micrographs used for statistical analysis of the various encapsulation states can be found in **Figure S3-S6**. The overall size of each particle containing increasing concentrations of PEG tether were analyzed using dynamic light scattering (**Figures S7-S8**), indicating similarly sized particles with a large size distribution, likely due to the remaining flexibility of the PEG tether despite increased concentration of DNA ligand as a backfill.

The trends shown in **Figure 4A-D** reflect that the relative distribution of encapsulation states that are predicted by the phase diagrams (**Figure 3**) and is consistent with the grafting densities of PEG tethered on the NP surfaces and the amount of free lipid added to the system.

These results show the predictive power of the simulation and provide a guide for how to obtain specific states of encapsulation when the stiffness of the underlying anchored polymer-lipid can be controlled.

2.3. Physical properties of TMLs

As discussed above, at all four different polymer persistence lengths, a perfectly encapsulated TML can always be made through self-assembly when situated in a suitable region as outlined within the phase diagrams (**Figure 3**). Herein, we will calibrate the physical properties of perfect encapsulated TMLs by calculating their radius, density distribution and the amount of stored water embedded within the templated lipid bilayer.

Size distribution. As given in **Figure 5 (A)**, the radii of perfectly encapsulated TMLs under different persistence lengths is shown as a function of the polymer grafting density. The radius is obtained by averaging the radii of perfectly encapsulated TMLs at a particular grafting density. There are two important things we can learn from **Figure 5 (A)**. First, with the same polymer persistence length, the radius of perfectly encapsulated TMLs slightly increases as the grafting density increases. For instance, at $\overline{l_p} = 0.17$, the radius of TMLs increases from $R = 9$ nm at $\sigma_g = 0.2/\text{nm}^2$ to $R = 11$ nm at $\sigma_g = 0.8/\text{nm}^2$. Similarly, at $\overline{l_p}$ $= 1.21$, the radius of TMLs increases from $R = 13.5$ nm at $\sigma_g = 0.5/\text{nm}^2$ to $R = 15$ nm at $\sigma_g = 0.8/\text{nm}^2$. However, this variation in size at each persistence length is no larger than 23 %, which indicates that the size of perfectly encapsulated TMLs can be well controlled by the nature of the tethered polymers. Second, the size of a perfectly encapsulated TML increases as the persistence length of tethered polymers increases. The averaged radii of the perfectly encapsulated TMLs are $R \approx 10, 11, 14, 16$ nm, respectively for persistence lengths of $\overline{l_p} =$ 0.17, 0.21, 1.21, 2.21.

Density distributions. After inspecting their size, we further investigated the structure of perfectly encapsulated TMLs by calculating the radial density distribution of each component.

In addition to the inorganic core, there are three different components within TMLs, including the tethered polymers, lipids and encapsulated water molecules. The density distribution in **Figure 5 (B)** is obtained from the perfectly encapsulated TML with a persistence length of $\overline{l_p}$ = 0.21. The corrsponding grafting density and free lipid number is $\sigma_g = 0.8/nm^2$ and N_f = 5500. The density distribution for the other perfectly encapsulated TMLs is very similar. As we can see from **Figure 5 (B)**, the density of tethered polymers decreases dramatically from the surface of the inorganic core from a distance of $D = 5$ nm to the radius of the entire TML at around 12 nm. At $D = 12$ nm, a lipid density peak appears, due to the lipid coverage on the surface. Since water is repelled from the lipid-containing region, its density can be divided into two separate regions. When $D > 12$ nm, the water density increases quickly from 0 to $3/nm^2$. This population of water molecules outside the TML is due to the hydrophobicity of the lipid bilayer core. When $D < 12$ nm, the water density starts increasing from $D = 5$ nm at the core surface and then drops quickly near the lipid bilayer shell. This portion of water molecules is encapsulated by the lipid bilayer and stored within the TMLs.

Stored water. The portion of stored water molecules inside TMLs represents the free space of the NP that can be used to load other hydrophilic molecules, including small drug molecules. To further explore the TMLs capacity for storing water, we calculated the amount of stored water for each polymer persistence length as a function of the grafting density. As given in **Figure 5 (C)**, for all the perfectly encapsulated TMLs, the number of stored water beads is on the order of 10^4. More importantly, consistent with the increment of the TML radius, the stored number of water molecules increases dramatically from 1×10^4 at $\overline{l_p}$ = 0.17 to 3.4×10^4 at $\overline{l_p} = 2.11$. A water bead in the DPD simulation is generally used to represent three water molecules [53]. Taking the volume of a water molecule as $3 \times 10^{-2} \ nm^3$, we can estimate that the free space of the TMLs ranges from 300 to 3000 nm^3, depending on the flexibility of tethered polymers.

14

2.4. Theoretical estimations on free lipid number and critical grafting density for perfectly encapsulated TMLs

As noted, a perfectly encapsulated TML can only form when a suitable amount of free lipids is present, and when the grafting density is optimal. In quantitative terms, the corresponding numbers are given by the free lipid number boundary and critical grafting density. In this part, we will explore the physical mechanism that determines the suitable range of these parameters within the phase diagrams of **Figure 3**.

Estimation of free lipid number. To estimate the suitable free lipid number, we will explore the parameters that determine the radius of a perfectly encapsulated TML. The free lipid number needed by a perfectly encapsulated TML should be determined by its radius R, whose relationship should be given as:

$$N_f^{\text{need}} \approx 2\frac{4\pi R^2}{a_p} \qquad (1)$$

where a_p is the area per lipid molecule. The next task is to determine the radius R of a perfectly encapsulated TML before the self-assembly process. At the perfectly encapsulated state, all the anchored lipids are inserted into the lipid bilayer shell. Therefore, the tethered polymers are confined within a region formed by the inorganic core and the lipid bilayer shell. If the radius of the lipid bilayer shell is too small, the tethered polymers will produce a large osmotic pressure that might cause the rupture of the lipid bilayer shell. On the other hand, if the radius of the lipid bilayer shell is too large, the tethered polymers will experience an extensive force. This would result in the anchored lipid being pulled out of the lipid bilayer. From this perspective, the radius of the lipid bilayer shell should be in a suitable region to prevent the large osmotic pressure and extensive force from tethered polymers.

To confirm our analysis and determine the relationship between the encapsulated TML radius and free energy state of the tethered polymers, we performed a test for tethered polymers as given in **Figure 6 (A)** and **(B)**. The free ends of the tethered polymers are confined within a spherical indenter surface. The terminal of each polymer can freely translate on the indenter

15

surface. The indenter surface produces a repulsive force acting on the monomers if these individual monomers reside outside the indenter surface. On the other hand, if the terminal monomer of a polymer chain is located inside of the indenter surface, the indent will produce an outward repulsive force. This way, the indenter surface can mimic the lipid bilayer shell and is able to measure both the osmotic pressure and extensive force. During this process, we systematically changed the radius of the indenter to investigate the variation of the tethered polymer energy against the possible radius of a perfectly encapsulated TML.

As given in **Figure 6 (C)** at the persistence length of $\bar{l}_p = 0.17$, the free energy of the tethered polymers is large for both the small and large indenter radii. At the smaller radius, the tethered polymers produce a large osmotic pressure. At the larger radius, the large free energy is caused by extension of tethered polymers. A low energy state appears in the radius range from 10 to 13 nm. This low energy region correlates extremely well with the perfectly encapsulated TML radii (9-11 nm) we obtained through self-assembly simulations. Similar low energy ranges are found for the tethered polymers with other persistence lengths. More importantly, if we take the optimal indenter radius as the region that is no larger than $5k_BT$ of its minimum value (marked by light shaded regions), the optimal radii are 10-13 nm, 11-13 nm, 14-16 nm and 15-16.4 nm, respectively for the normalized persistence lengths $\bar{l}_p = 0.17, 0.21, 1.21,$ and 2.2. This low energy state range at each persistence length is consistent with the radius of perfectly encapsulated TMLs. Therefore, we can conclude that the radii of perfectly encapsulated TMLs are mainly determined by the free energy of the tethered polymers. The self-assembly process finally results in a perfectly encapsulated TML at the most favorable energy state for the tethered polymers.

More importantly, if we take the area per lipid a_p as 0.7 nm^2 as given in the **Figure S9** of the Supporting Information, the suitable free lipid number for each persistence length is around $(3.6\text{-}6.1) \times 10^3$, $(4.3\text{-}6.1) \times 10^3$, $(7.0 - 9.2) \times 10^3$ and $(8.1\text{-}9.7) \times 10^3$, based on the

relationship in Equation 1. All of these estimated values are located within the perfectly

encapsulated region as given in the phase diagram (**Figure 3**). Therefore, as long as the

persistence length of tethered polymers is given, we are able to estimate its perfectly

encapsulated size in simulation and evaluate the required number of free lipids using Equation

1.

Estimation of critical grafting density. The next question is how to determine the critical

grafting density for a perfectly encapsulated TML. Based on the phase diagrams in **Figure 3**,

the critical grafting density increases as the tethered polymers become stiffer. As we

discussed above, the key driving force during the self-assembly process is that the anchored

lipids attract surrounding free lipids, which contributes to the fusion between anchored

vesicles/bilayer patches. Based on what we have learned from the planar tethered lipid bilayer

membrane, we know that the density of anchored lipids should be larger than a critical value,

σ_{pc} [54,55]. For our TMLs, the radius of the polymer tethered core increases with increasing

polymer stiffness. This increment of size reduces the effective density of anchored lipids.

Taking the spherical geometry into account, the critical grafting density σ_{crit} of the perfectly

encapsulated TMLs should obey the following relationship as [56]:

$$\sigma_{\text{crit}} \approx \sigma_{pc}\left(\frac{R_{\text{NP}}}{R_{\text{Core}}}\right)^2 \qquad (2)$$

where R_{NP} and R_{Core} are the radii of a perfectly encapsulated TML and the inorganic core,

respectively. To confirm our analysis, we further investigated the self-assembly process of a

planar substrate with tethered polymers of different stiffness. To form a perfect planar

tethered bilayer on the terminals of tethered polymers, the free lipid number can be estimated

through the lipid area and the size of substrate as given in **Figure 6 (D)**. Here, the substrate

size is $(50 \times 50)\,\text{nm}^2$. The free lipid number is 7000. As shown in **Figure 6 (D)**, the self-

assembly process of the planar substrate is quite similar to that of the aforementioned TMLs.

The formation of the planar tethered lipid bilayer is mainly determined by fusion between

anchored vesicles and bilayer patches. By systematically changing the grafting density of tethered polymers, we find that the critical grafting density of polymers with persistence lengths of $\overline{l_p} = 0.21$, 1.21, 2.21 is insensitive to stiffness, with a value about $\sigma_{pc} = 0.06/\text{nm}^2$. The σ_{pc} for $\overline{l_p} = 0.17$ is slightly smaller with a value around 0.04 /nm^2 (refer to the Supporting Information for more details, **Figure S11-S14**). If one takes the σ_{pc} of planar tethered lipid bilayer as 0.06 /nm^2 and inserts it into Equation 2, one obtains the relationship between the critical grafting density σ_{crit} of a perfectly encapsulated TML and the ratio $R_{\text{NP}}/R_{\text{Core}}$, as given in **Figure 6 (E)**. Interestingly, we find that the data points obtained from the phase diagram and the TML radii are consistent with the curve resulting from Equation 2. The critical grafting density σ_{crit} of tethered polymers can therefore be directly estimated by Equation 2.

Table 1. Comparison of boundary values for perfectly encapsulated TMLs between simulation and theory.

	$\overline{l_p} = 0.17$	$\overline{l_p} = 0.21$	$\overline{l_p} = 1.21$	$\overline{l_p} = 2.21$
Boundary values from simulation results				
Lower free lipid number ($\times 10^3$)	3.0-4.5	3.0-4.5	5.5-7.0	6.5-7.5
Upper free lipid number ($\times 10^3$)	4.5-6.5	5.0-7.0	8.5-9.5	9.5-10.5
Grafting density $(1/nm^2)$	0.05-0.20	0.20-0.35	0.35-0.50	0.35-0.50
Boundary values from theoretical predictions				
Lower free lipid number ($\times 10^3$)	3.6	4.3	7.0	8.1
Upper free lipid number ($\times 10^3$)	6.1	6.1	9.2	9.7
Grafting density $(1/nm^2)$	0.20	0.24	0.43	0.58

To summarize this analysis as it relates to the free energy state of tethered polymers, the radius of the perfectly encapsulated TMLs increases as the polymer stiffness increases. The

radius of the perfectly encapsulated TML at a given polymer persistence length can be evaluated through an indenter test in simulations, which is a time-saving alternative to the self-assembly simulations. As soon as the radius of a perfectly encapsulated TML is determined, its optimal free lipid number and critical grafting density can both be estimated from Equations 1 and 2. Based on Equation 2, it is also interesting to note that the increment of the inorganic core radius will reduce the critical grafting density, as observed in the self-assembly of TML (with R=5 *nm*) and planar tethered bilayer (with R= ∞). Here, we also need to mention that the direct relation between the polymer stiffness and brush height of the tethered polymer at most favorable energy state requires additional systematically works, which will be explored in our further study. As listed in **Table 1**, the theoretical predictions agree well with the simulation results regarding the lower and upper free lipid boundaries and grafting density boundary. In summary, we here provided and tested an efficient way to predict the free lipid number and critical grafting density for synthesizing TMLs using tethered polymers with variable degree of semiflexibility.

3. CONCLUSION

In this work, we proposed that the self-assembly of TMLs can be utilized as a general approach to produce liposomes with controlled sizes using tethered polymers of varying stiffness. To confirm this, large scale molecular simulations were performed and used to investigate the self-assembly process of TMLs in the presence of four types of tethered polymers that differ in their persistence lengths. For each type, a phase diagram was established that describes the self-assembled structures as a function of free lipid number and polymer grafting density. Three different states, including partially encapsulated, perfectly encapsulated, and over encapsulated TMLs are featured in each of the phase diagrams. It is found that the perfectly encapsulated TMLs can only be created under conditions of optimal polymer grafting density and suitable free lipid number, which in turn depend on the degree

of semiflexibility. To support our simulation findings, experimental validations were undertaken. In these experiments, we synthesized DNA-PEG CPLS NPs upon incorporating increasing concentrations of DNA as a proxy for increasing the rigidity of the tethered polymer layer. Using transmission electron microscopy analysis we confirmed that the resulting structures exhibit degrees of encapsulation by free lipids that are consistent with the corresponding simulations. Further analysis of the properties of the perfectly encapsulated TML case showed that the radius of a TML is well controlled by the flexibility of tethered polymers. To provide a better understanding and a general guidance for synthesizing a perfectly encapsulated TML, a numerical indenter test was proposed that allows to estimate the radius of a TML. We found that the radius of a perfectly encapsulated TML is determined by the lowest free energy state of the tethered polymers. More importantly, analytical expressions are provided to directly estimate the required free lipid number and critical grafting density for given persistence length and polymerization degree of the tethered polymer. Through these combined computational, experimental and theoretical studies, we ended up with a seemingly powerful predictive model for determining the effect of polymer stiffness on the self-assembly of TMLs. In addition, the polymerization degree of tethered polymers can be further tuned to control the sizes and loading capacities of these TMLs. It may potentially be used as a general approach to obtain perfectly encapsulated TMLs as potential drug delivery vehicles.

4. METHODS

4.1. Computational model and method

Dissipative particle dynamics (DPD) method. The DPD method is a coarse-grained molecular simulation method which can correctly and accurately capture hydrodynamic behavior [57,58]. The basic interacting sites in DPD simulations are soft beads. Between each pair of DPD beads, effective two-body interactions consist of three major forces: a conservative force $\boldsymbol{F}^{C}$, a random

force $\boldsymbol{F}^R$, and a dissipative force $\boldsymbol{F}^D$. Specifically, the conservative force between beads i and j is

$\boldsymbol{F}_{ij}^C = a_{ij}\omega(r_{ij})\boldsymbol{e}_{ij}$, where r_{ij} denotes the spatial distance between beads i and j, and $\boldsymbol{e}_{ij}$ the unit vector

pointing from bead i to bead j; a_{ij} represents the maximum repulsive force strength acting between

beads i and j. The weighting factor $\omega(r_{ij})$ is a normalized distribution function as $\omega(r_{ij}) = 1 - r_{ij}/$

r_0 for $r_{ij} \leq r_0$, while $\omega(r_{ij}) = 0$ for $r_{ij} > r_0$. Here r_0 is the cutoff distance for pairwise interactions.

The random force $\boldsymbol{F}_{ij}^R = \sqrt{2\gamma k_B T/\Delta t}\,\omega(r_{ij})\alpha\boldsymbol{e}_{ij}$, where α represents a normal distributed Gaussian

random number with zero mean and unit variance. Δt is the time step used in the molecular

simulations, k_B and T denote the Boltzmann constant and temperature, respectively, and γ is a bead

friction coefficient. The dissipative force is $\boldsymbol{F}_{ij}^D = -\gamma\omega^2(r_{ij})(\boldsymbol{e}_{ij} \cdot \boldsymbol{v}_{ij})\boldsymbol{e}_{ij}$, where $\boldsymbol{v}_{ij}$ represents the

relative velocity vector between beads i and j.

Lipid molecule model. A linear chain model is taken for each lipid molecule for simplicity and its

efficiency. A lipid molecule in our simulation contains one hydrophilic head (H) bead and three

hydrophobic tail (T) heads denoted as HT_3. The amphiphilic properties of the lipids are ensured by

a large repulsion between the lipid tail and water molecule, using $a_{tw} = 100\ k_B T/r_0$. The subscript

letters 't' and 'w' denote the lipid tail and water bead, respectively. The lipid heads are hydrophilic

and thus $a_{hw} = 25\ k_B T/r_0$, where the subscript 'h' represents the lipid head beads. The remaining

pairwise interaction parameters between the same types of beads are $a_{ww} = a_{hh} = a_{hh} = 25 k_B T/r_0$.

Apart from the pairwise interactions, bond and angle potentials are applied to the lipid molecules to

correctly reproduce their conformations. The neighboring beads in a lipid molecule are connected

by a harmonic spring potential: $U_{s1} = K_{s1}(r_{ij} - r_{s1})^2$, where K_{s1} and r_{s1} are the spring coefficient

and equilibrium bond length, respectively. Here $K_{s1} = 50\ k_B T/r_0^2$. and $r_{s1} = 0.7\ r_0$. A bond angle

potential is applied to the lipid tail to ensure its rigidity and to prevent the incorrect interaction in

the middle plane of the self-assembled bilayer. The form of the bond angle potential is given by

$U_{\theta 1} = K_{\theta 1}(\theta - \theta_{01})^2$, where $K_{\theta 1}$ and θ_{01} are the bending stiffness and equilibrium angle,

respectively. Here $K_\theta = 3.0\ k_B T$ and $\theta_0 = 180°$. Under these interactions, the random lipid

molecules are able to self-assemble into a vesicle or a planar membrane under suitable concentrations [59,60].

Polymer and nanoparticle model. All polymer chains tethered on the inorganic core have the same polymerization degree of $N=30$. The monomers within a polymer are connected by a harmonic bond potential: $U_{s2} = K_{s2}(r_{ij} - r_{s2})^2$, with spring stiffness $K_{s2} = 2111.3\ k_BT/r_0^2$ and equilibrium distance $r_{s2} = 0.4125\ r_0$. Additionally, an angular potential, defined as $U_{\theta2} = K_{\theta2}(\cos\theta - \cos\theta_{02})^2$, is applied between three consecutive monomers to tune the stiffness of polymer. To be specific, when $K_{\theta2} = 16.4946\ k_BT$ and equilibrium angle $\theta_{02} = 130°$, the polymer can correctly reproduce the conformation of a PEG polymer in water [61-63]. Three additional angular constants, $K_{\theta2} = 0, 100, 500\ k_BT$ are used to model polymers with different stiffness. The equilibrium angles in these three cases are taken as $\theta_{02} = 180°$. To calibrate the polymer stiffness, we calculate the polymer persistence length under these parameters. Four different persistence lengths of $\overline{l_p} = 0.17, 0.21, 1.21, 2.21$ are obtrained for the angular constants of $K_{\theta2} = 0$, $16.4946, 100,$ and $500\ k_BT$, respectively. Please refer to the Supporting information for details about the estimation of polymer persistence length. In order to take the flexible linker between the inorganic core and tethered polymer, the angular constant for the angle potential relating the bead on inorganic core and the first two beads in each polymers is taken as zero.

The inorganic core is represented by a rigid NP and corresponding beads are arranged on a FCC lattice with a lattice parameter $0.8\ r_0$, covered by a layer of spherical shell beads. There are 1575 beads in total for the core with a radius of $5\ r_0$. A polymer is grafted on the surface of the rigid core through a harmonic potential. The grafting density σ_g of the tethered polymer in our DPD simulations is 0.05, 0.2, 0.35, 0.5, 0.65, and 0.8 chains per r_0^2. The corresponding numbers of polymer chains is $M = 15, 63, 110, 157, 204$ and 251, respectively. All free ends of the grafted polymers are bonded with lipid (head) molecules through a harmonic potential. For simplicity, we assume that this harmonic potential is the same as that for polymers. In this way, one end of the

polymer is tethered on the core surface, while the other end is covalently connected to a lipid molecule.

Simulation protocol.   All the repulsive interaction parameters a_{ij} for different types of beads are given in **Table S1** of the Supporting Information. Periodic boundary conditions are applied along all directions. The number density of beads in the simulation box is fixed at $3/r_0^3$ [57]. The physical length corresponding to our simulation units are obtained by comparing the membrane thickness in simulations $d_{\mathrm{HH}} = 3.4\ r_0$ to the thickness of a DMPC membrane, $d_{\mathrm{HH}} \approx 3.53$ nm [64], indicating $r_0 \approx 1$ nm. The experimental lipid lateral diffusion coefficient of DMPC [65] is $D \approx 5 \mu\mathrm{m}^2\mathrm{s}^{-1}$. The lipid lateral diffusion coefficient in simulation is, $D_{\mathrm{lipid}} \approx 5.59 \times 10^{-2} r_0^2/\tau$. Therefore, we estimate the physical time scale $\tau = 11.2$ ns.

4.2 Synthesis and Characterization of CPLS-PEG-DNA NPs

Synthesis of CPLS NPs with DNA backfill.

Materials.   DNA oligomer was synthesized in house using reagents purchased from Glen Research. Gold(III) chloride trihydrate, sodium citrate tribasic dihydrate, dithiothreitol, 30% ammonium hydroxide and 1,2-dioleoyl-sn-glycero-3-phosphoethanolamine (DOPE) were purchased from Millipore-Sigma. 5000 molecular weight 1,2-distearyl-sn-glycero-3-phosphoethanolamine-polyethylene glycol-thiol (DSPE-PEG-SH) was purchased from NanoCS. NAP-5 Sephadex columns were purchased from GE Healthcare.

Synthesis of Au NPs.   30nm Au NPs were synthesized through citrate reduction. 13.8 mg of gold(III) chloride trihydrate were diluted to 49 mL in water. 43.8 mg of sodium citrate tribasic dihydrate were diluted to 1 mL in water. The gold solution was heated until refluxing with constant stirring. The citrate solution was added via syringe to the gold solution. The mixture was incubated while refluxing for 30 minutes. The resulting citrate capped Au NP solution was filtered through a 0.22 μm PTFE filter.

Synthesis of DNA oligomer. DNA was synthesized through standard phosphoramidite coupling chemistry using an automated DNA synthesizer. A polyT 20 DNA sequence was synthesized on a 3'-thiol-modifier- 6 S-S CPG. The DNA was cleaved at room temperature using 30% ammonium hydroxide and the resulting solution was deprotected at 55 °C for 18 hours. The ammonium hydroxide was removed under vacuum and redissolved in water. The resulting solution was then purified through a NAP-5 Sephadex column.

Synthesis of Polymer Tethered Core NPs. Ligands were added to the citrate capped Au NPs in a 10,000:1 molar ratio. The DNA was treated with dithiothreitol for 30 minutes and purified using a NAP-5 Sephadex column. DSPE-PEG-SH was weighed out under an inert atmosphere in a glovebox and diluted to 500 µl with ethanol. The DNA and DSPE-PEG-SH were combined together prior to adding to the Au NPs. The resulting solutions were added to the Au NPs and diluted to 300 µl with water. These were sonicated for 1 hour. After sonication, samples were diluted to 746 µl with water. These were incubated on a rotisserie for 1 hour at room temperature. 1.25 µl of 2 mM sodium chloride solution was then added to each sample and were allowed to mix on the rotisserie overnight at room temperature. 1.25 µl of 2 mM sodium chloride was then added and allowed to incubate for an hour. The samples were then washed by pelleting on a centrifuge at 9,400 x g for 30 minutes one time. Resulting samples were immediately encapsulated with free lipid.

Free Lipid Encapsulation. Using a gas tight syringe, 15 µl of 130 µM DOPE was added to a 1.5 mL microcentrifuge tube for each sample. Chloroform solvent was allowed to evaporate, forming a thin film. The functionalized Au NPs were pelleted using a centrifuge at 9,400 x g for 30 minutes, the supernatant was removed until a 30 µl volume remained. The Au NPs were briefly sonicated to mix, and added to the DOPE thin film. The solution was then sonicated for 1 hour.

Nanoparticle Characterization. Samples were dropcast on a 400 mesh Cu grid with carbon formvar coating (Electron Microscopy Sciences). All samples were stained with 0.5% uranyl acetate prior to imaging. Transmission Electron Microscopy (TEM) images were taken on a

ThermoFisher Tecnai 12 G2 Spirit BioTWIN TEM with an accelerating voltage of 120 keV. Dynamic light scattering measurements observed on a Malvern Zetasizer ZS90.

Supporting Information
Supporting Information is available for computational model setup and protocol, and additional simulation and experimental results.

DATA AVAILABILITY

The data that support the findings of this study are available from the corresponding author upon reasonable request.

ACKNOWLEDGEMENTS

AUTHOR CONTRIBUTIONS

Y.L., Z.S. and J.R. contributed to the design of the research. Y.L., Z.S., A.F. and M.K. contributed to the computational and theoretical studies of the research. D.L. and J.R. contributed to the experimental studies of the research. All the authors contributed to the analysis of the results and to the writing of the manuscript.

ADDITIONAL INFORMATION

Competing interests: The authors declare no competing interests.

REFERENCES

1   Kim, B. Y., Rutka, J. T. & Chan, W. C. Nanomedicine. *New England Journal of Medicine* **363**, 2434-2443 (2010).
2   Davis, M. E. *et al.* Evidence of RNAi in humans from systemically administered siRNA via targeted nanoparticles. *Nature* **464**, 1067 (2010).
3   Nie, S. Understanding and overcoming major barriers in cancer nanomedicine. *Nanomedicine* **5**, 523-528 (2010).
4   Soppimath, K. S., Aminabhavi, T. M., Kulkarni, A. R. & Rudzinski, W. E. Biodegradable polymeric nanoparticles as drug delivery devices. *Journal of controlled release* **70**, 1-20 (2001).
5   Cho, K., Wang, X., Nie, S. & Shin, D. M. Therapeutic nanoparticles for drug delivery in cancer. *Clinical cancer research* **14**, 1310-1316 (2008).
6   Rosi, N. L. *et al.* Oligonucleotide-modified gold nanoparticles for intracellular gene regulation. *Science* **312**, 1027-1030 (2006).
7   Walkey, C. D., Olsen, J. B., Guo, H., Emili, A. & Chan, W. C. Nanoparticle size and surface chemistry determine serum protein adsorption and macrophage uptake. *Journal of the American Chemical Society* **134**, 2139-2147 (2012).
8   Chou, L. Y., Ming, K. & Chan, W. C. Strategies for the intracellular delivery of nanoparticles. *Chemical Society Reviews* **40**, 233-245 (2011).
9   Ke, P. C., Lin, S., Parak, W. J., Davis, T. P. & Caruso, F. A decade of the protein corona. *ACS nano* **11**, 11773-11776 (2017).
10   Shen, Z., Nieh, M.-P. & Li, Y. Decorating nanoparticle surface for targeted drug delivery: opportunities and challenges. *Polymers* **8**, 83 (2016).
11   Li, Y. *et al.* Cell and nanoparticle transport in tumour microvasculature: the role of size, shape and surface functionality of nanoparticles. *Interface focus* **6**, 20150086 (2016).
12   Albanese, A., Tang, P. S. & Chan, W. C. The effect of nanoparticle size, shape, and surface chemistry on biological systems. *Annual review of biomedical engineering* **14**, 1-16 (2012).
13   Wilhelm, S. *et al.* Analysis of nanoparticle delivery to tumours. *Nature reviews materials* **1**, 16014 (2016).

14   Rosenblum, D., Joshi, N., Tao, W., Karp, J. M. & Peer, D. Progress and challenges towards targeted delivery of cancer therapeutics. *Nature communications* **9**, 1410 (2018).

15   Lian, T. & Ho, R. J. Trends and developments in liposome drug delivery systems. *Journal of pharmaceutical sciences* **90**, 667-680 (2001).

16   Sharma, A. & Sharma, U. S. Liposomes in drug delivery: progress and limitations. *International journal of pharmaceutics* **154**, 123-140 (1997).

17   Pattni, B. S., Chupin, V. V. & Torchilin, V. P. New developments in liposomal drug delivery. *Chemical reviews* **115**, 10938-10966 (2015).

18   Krishnamurthy, S., Vaiyapuri, R., Zhang, L. & Chan, J. M. Lipid-coated polymeric nanoparticles for cancer drug delivery. *Biomaterials science* **3**, 923-936 (2015).

19   Kraft, J. C., Freeling, J. P., Wang, Z. & Ho, R. J. Emerging research and clinical development trends of liposome and lipid nanoparticle drug delivery systems. *Journal of pharmaceutical sciences* **103**, 29-52 (2014).

20   Torchilin, V. P. Recent advances with liposomes as pharmaceutical carriers. *Nature reviews Drug discovery* **4**, 145 (2005).

21   Barenholz, Y. C. Doxil®—the first FDA-approved nano-drug: lessons learned. *Journal of controlled release* **160**, 117-134 (2012).

22   Huang, C.-H. Phosphatidylcholine vesicles. Formation and physical characteristics. *Biochemistry* **8**, 344-352 (1969).

23   Olson, F., Hunt, C., Szoka, F., Vail, W. & Papahadjopoulos, D. Preparation of liposomes of defined size distribution by extrusion through polycarbonate membranes. *Biochimica et Biophysica Acta (BBA)-Biomembranes* **557**, 9-23 (1979).

24   Silva, R., Ferreira, H., Little, C. & Cavaco-Paulo, A. Effect of ultrasound parameters for unilamellar liposome preparation. *Ultrasonics sonochemistry* **17**, 628-632 (2010).

25   van Swaay, D. Microfluidic methods for forming liposomes. *Lab on a Chip* **13**, 752-767 (2013).

26   Jousma, H. *et al.* Characterization of liposomes. The influence of extrusion of multilamellar vesicles through polycarbonate membranes on particle size, particle size distribution and number of bilayers. *International Journal of Pharmaceutics* **35**, 263-274 (1987).

27   Costa, A. P., Xu, X., Khan, M. A. & Burgess, D. J. Liposome Formation Using a Coaxial Turbulent Jet in Co-Flow. *Pharmaceutical research* **33**, 404-416 (2016).

28   Tanasescu, R. *et al.* Vesicle origami and the influence of cholesterol on lipid packing. *Langmuir* **32**, 4896-4903 (2016).

29   Genç, R. k., Ortiz, M. & O′ Sullivan, C. K. Curvature-tuned preparation of nanoliposomes. *Langmuir* **25**, 12604-12613 (2009).

30   Sykes, E. A. *et al.* Tailoring nanoparticle designs to target cancer based on tumor pathophysiology. *Proceedings of the National Academy of Sciences* **113**, E1142-E1151 (2016).

31   Dai, Q. *et al.* Quantifying the ligand-coated nanoparticle delivery to cancer cells in solid tumors. *ACS nano* **12**, 8423-8435 (2018).

32   Chithrani, B. D., Ghazani, A. A. & Chan, W. C. Determining the size and shape dependence of gold nanoparticle uptake into mammalian cells. *Nano letters* **6**, 662-668 (2006).

33   Gao, H., Shi, W. & Freund, L. B. Mechanics of receptor-mediated endocytosis. *Proceedings of the National Academy of Sciences* **102**, 9469-9474 (2005).

34   Shen, Z., Ye, H., Yi, X. & Li, Y. Membrane Wrapping Efficiency of Elastic Nanoparticles during Endocytosis: Size and Shape Matter. *ACS nano* **13**, 215-228 (2018).

35   Yang, Y. *et al.* Self-assembly of size-controlled liposomes on DNA nanotemplates. *Nature chemistry* **8**, 476 (2016).

36   Shen, Z. *et al.* Self-assembly of core-polyethylene glycol-lipid shell (CPLS) nanoparticles and their potential as drug delivery vehicles. *Nanoscale* **8**, 14821-14835 (2016).

37   Shen, Z., Ye, H., Kröger, M. & Li, Y. Self-assembled core–polyethylene glycol–lipid shell nanoparticles demonstrate high stability in shear flow. *Physical Chemistry Chemical Physics* **19**, 13294-13306 (2017).

38   Shen, Z., Fisher, A., Liu, W. K. & Li, Y. in *Engineering of Biomaterials for Drug Delivery Systems*   1-26 (Elsevier, 2018).

39   Cutler, J. I., Auyeung, E. & Mirkin, C. A. Spherical nucleic acids. *Journal of the American Chemical Society* **134**, 1376-1391 (2012).

40   Jensen, S. A. *et al.* Spherical nucleic acid nanoparticle conjugates as an RNAi-based therapy for glioblastoma. *Science translational medicine* **5**, 209ra152-209ra152 (2013).

41   Zheng, D. *et al.* Topical delivery of siRNA-based spherical nucleic acid nanoparticle conjugates for gene regulation. *Proceedings of the National Academy of Sciences* **109**, 11975-11980 (2012).

42   Giljohann, D. A. *et al.* Oligonucleotide loading determines cellular uptake of DNA-modified gold nanoparticles. *Nano letters* **7**, 3818-3821 (2007).

43   Seferos, D. S., Prigodich, A. E., Giljohann, D. A., Patel, P. C. & Mirkin, C. A. Polyvalent DNA nanoparticle conjugates stabilize nucleic acids. *Nano letters* **9**, 308-311 (2008).

44   Massich, M. D. *et al.* Regulating Immune Response Using Polyvalent Nucleic Acid−Gold Nanoparticle Conjugates. *Molecular pharmaceutics* **6**, 1934-1940 (2009).

45   Kapadia, C. H., Melamed, J. R. & Day, E. S. Spherical nucleic acid nanoparticles: Therapeutic potential. *BioDrugs* **32**, 297-309 (2018).

46   Chinen, A. B., Ferrer, J. R., Merkel, T. J. & Mirkin, C. A. Relationships between Poly (ethylene glycol) Modifications on RNA–Spherical Nucleic Acid Conjugates and Cellular Uptake and Circulation Time. *Bioconjugate chemistry* **27**, 2715-2721 (2016).

47   Wu, X. A., Choi, C. H. J., Zhang, C., Hao, L. & Mirkin, C. A. Intracellular fate of spherical nucleic acid nanoparticle conjugates. *Journal of the American Chemical Society* **136**, 7726-7733 (2014).

48   Chernomordik, L. V. & Kozlov, M. M. Mechanics of membrane fusion. *Nature structural & molecular biology* **15**, 675 (2008).

49   Zwanikken, J. W., Guo, P., Mirkin, C. A. & Olvera de la Cruz, M. Local ionic environment around polyvalent nucleic acid-functionalized nanoparticles. *The Journal of Physical Chemistry C* **115**, 16368-16373 (2011).

50   Li, T. I., Sknepnek, R., Macfarlane, R. J., Mirkin, C. A. & Olvera de la Cruz, M. Modeling the crystallization of spherical nucleic acid nanoparticle conjugates with molecular dynamics simulations. *Nano letters* **12**, 2509-2514 (2012).

51   Di Michele, L. & Eiser, E. Developments in understanding and controlling self assembly of DNA-functionalized colloids. *Physical Chemistry Chemical Physics* **15**, 3115-3129 (2013).

52   Hurst, S. J., Lytton-Jean, A. K. & Mirkin, C. A. Maximizing DNA loading on a range of gold nanoparticle sizes. *Anal. Chem.* **78**, 8313-8318 (2006).

53   Groot, R. D. & Rabone, K. Mesoscopic simulation of cell membrane damage, morphology change and rupture by nonionic surfactants. *Biophysical journal* **81**, 725-736 (2001).

54   McGillivray, D. J. *et al.* Molecular-scale structural and functional characterization of sparsely tethered bilayer lipid membranes. *Biointerphases* **2**, 21-33 (2007).

55   Wang, S. & Larson, R. G. Coarse-grained molecular dynamics simulation of tethered lipid assemblies. *Soft Matter* **9**, 480-486 (2013).

56   Hu, M., Stanzione, F., Sum, A. K., Faller, R. & Deserno, M. Design principles for nanoparticles enveloped by a polymer-tethered lipid membrane. *ACS nano* **9**, 9942-9954 (2015).

57   Groot, R. D. & Warren, P. B. Dissipative particle dynamics: Bridging the gap between atomistic and mesoscopic simulation. *The Journal of chemical physics* **107**, 4423-4435 (1997).

58   Hoogerbrugge, P. & Koelman, J. Simulating microscopic hydrodynamic phenomena with dissipative particle dynamics. *EPL (Europhysics Letters)* **19**, 155 (1992).

59   Shillcock, J. C. & Lipowsky, R. Equilibrium structure and lateral stress distribution of amphiphilic bilayers from dissipative particle dynamics simulations. *The Journal of chemical physics* **117**, 5048-5061 (2002).

60   Laradji, M. & Kumar, P. S. Dynamics of domain growth in self-assembled fluid vesicles. *Physical review letters* **93**, 198105 (2004).

61   Li, Y., Kröger, M. & Liu, W. K. Endocytosis of PEGylated nanoparticles accompanied by structural and free energy changes of the grafted polyethylene glycol. *Biomaterials* **35**, 8467-8478 (2014).

62   Li, Y., Kröger, M. & Liu, W. K. Shape effect in cellular uptake of PEGylated nanoparticles: comparison between sphere, rod, cube and disk. *Nanoscale* **7**, 16631-16646 (2015).

63   Shen, Z., Ye, H., Kröger, M. & Li, Y. Aggregation of polyethylene glycol polymers suppresses receptor-mediated endocytosis of PEGylated liposomes. *Nanoscale* **10**, 4545-4560 (2018).

64   Kučerka, N. *et al.* Structure of fully hydrated fluid phase DMPC and DLPC lipid bilayers using X-ray scattering from oriented multilamellar arrays and from unilamellar vesicles. *Biophysical journal* **88**, 2626-2637 (2005).

65   Orädd, G., Lindblom, G. & Westerman, P. W. Lateral diffusion of cholesterol and dimyristoylphosphatidylcholine in a lipid bilayer measured by pulsed field gradient NMR spectroscopy. *Biophysical journal* **83**, 2702-2704 (2002).
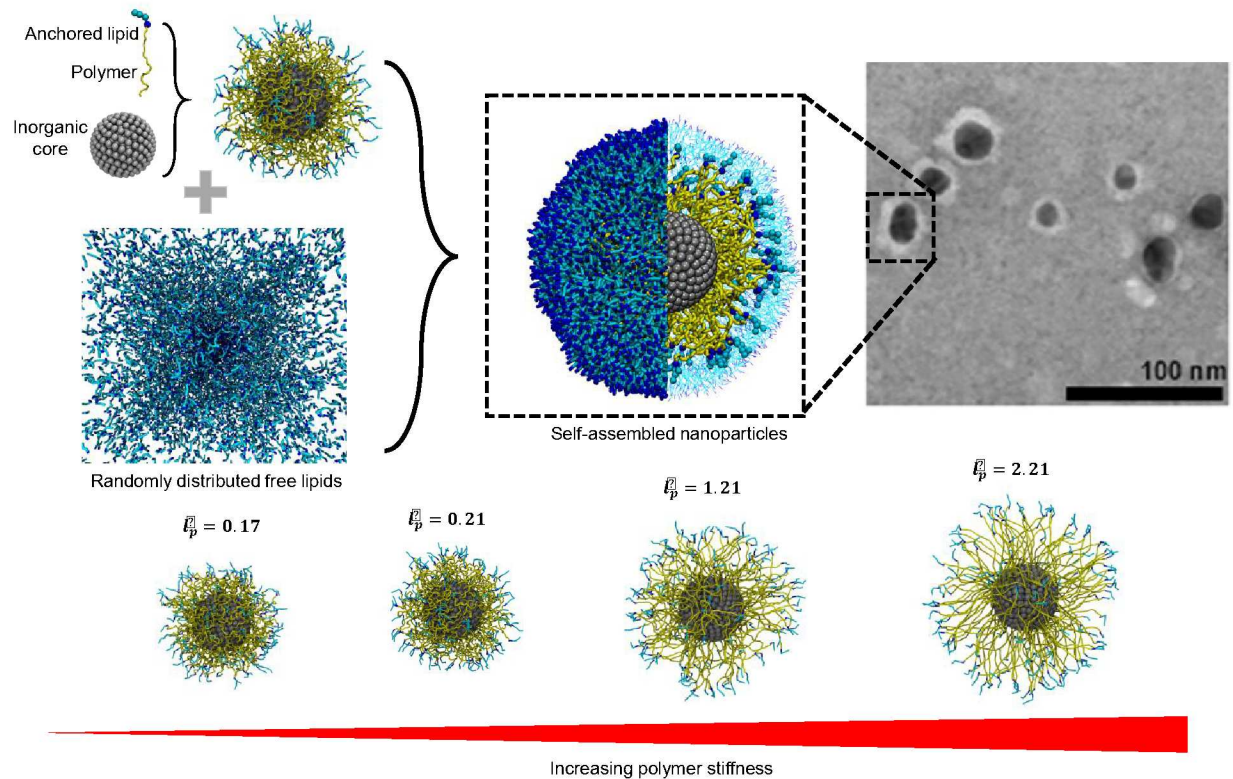
Figure 1. Schematic of the self-assembly of a TML. The spherical inorganic core is surface functionalized by polymer chains displaying anchored lipids at terminals. Upon addition of free lipid molecules around the polymer tethered core, a complete lipid bilayer shell forms at the surface, driven by the hydrophobic nature of lipid tails. The inorganic core is colored in silver, which could represent gold, superparamagnetic iron oxide or other materials. The polymer is colored yellow. The lipid heads and tails are colored in blue and cyan, respectively. Note that the free ends of the polymer are covalently bonded to the heads of anchored lipids. The lower panel shows the configurations of the polymer tethered cores at a series of different polymer persistence lengths.
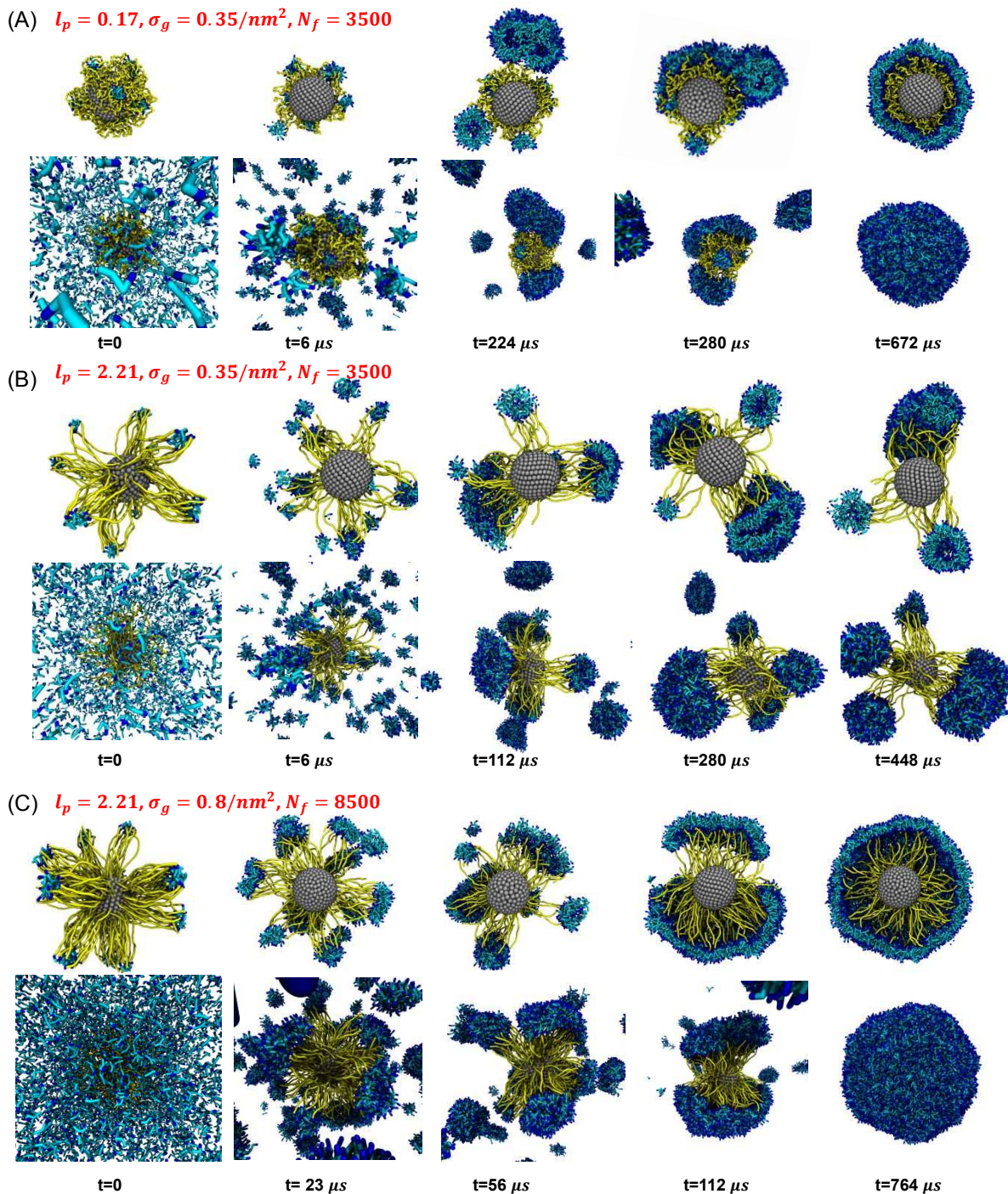
Figure 2. Self-assembly of TMLs at different stiffness of the tethered polymers. (A-B) Self-assembly process of TMLs with different normalized persistence lengths of $\overline{l_p} = 0.17$ and $\overline{l_p} = 2.21$. The grafting density and free lipid number are the same for both cases with values of $\sigma_g = 0.35 \, /nm^2$ and $N_f = 3500$. (C) Self-assembly process of TML with $\overline{l_p} = 2.21$, $\sigma_g = 0.8 \, /nm^2$ and $N_f = 8500$. The upper and lower panels in each figure show the whole and cross-sectional views respectively. Water beads are not shown for clarity.
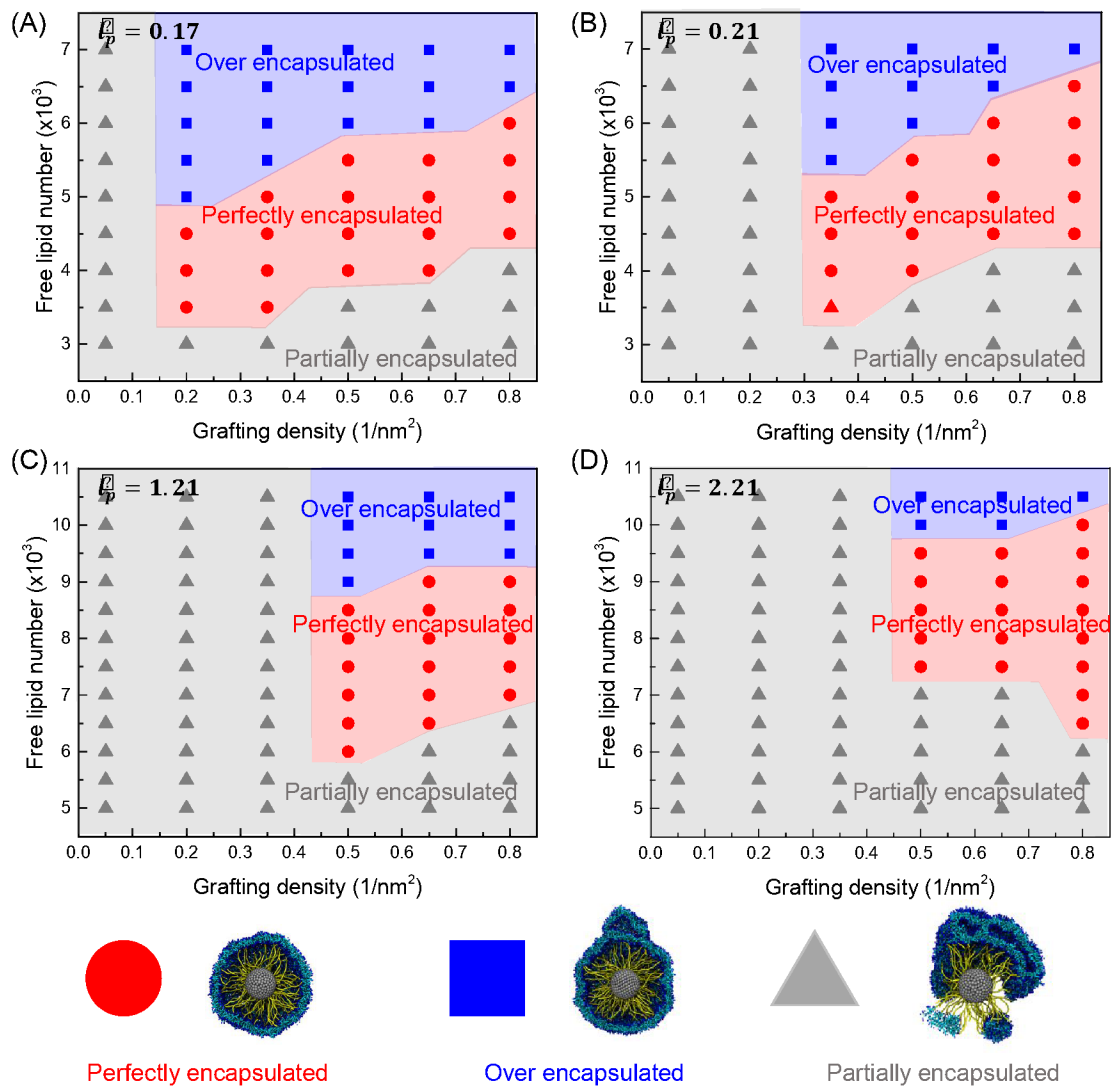
Figure 3. Phase diagrams of TMLs with tethered polymers of different stiffness. (A-D) Phase diagrams for TMLs with tethered polymers of normalized persistence lengthsl_p $= 0.17, 0.21, 1.21, and\ 2.21$, respectively. Each phase diagram is constructed as a function of free lipid number and grafting density. The results in each diagram can be classified into three different phases exhibiting (1) perfectly encapsulated states, (2) over encapsulated states, and (3) partially encapsulated states.
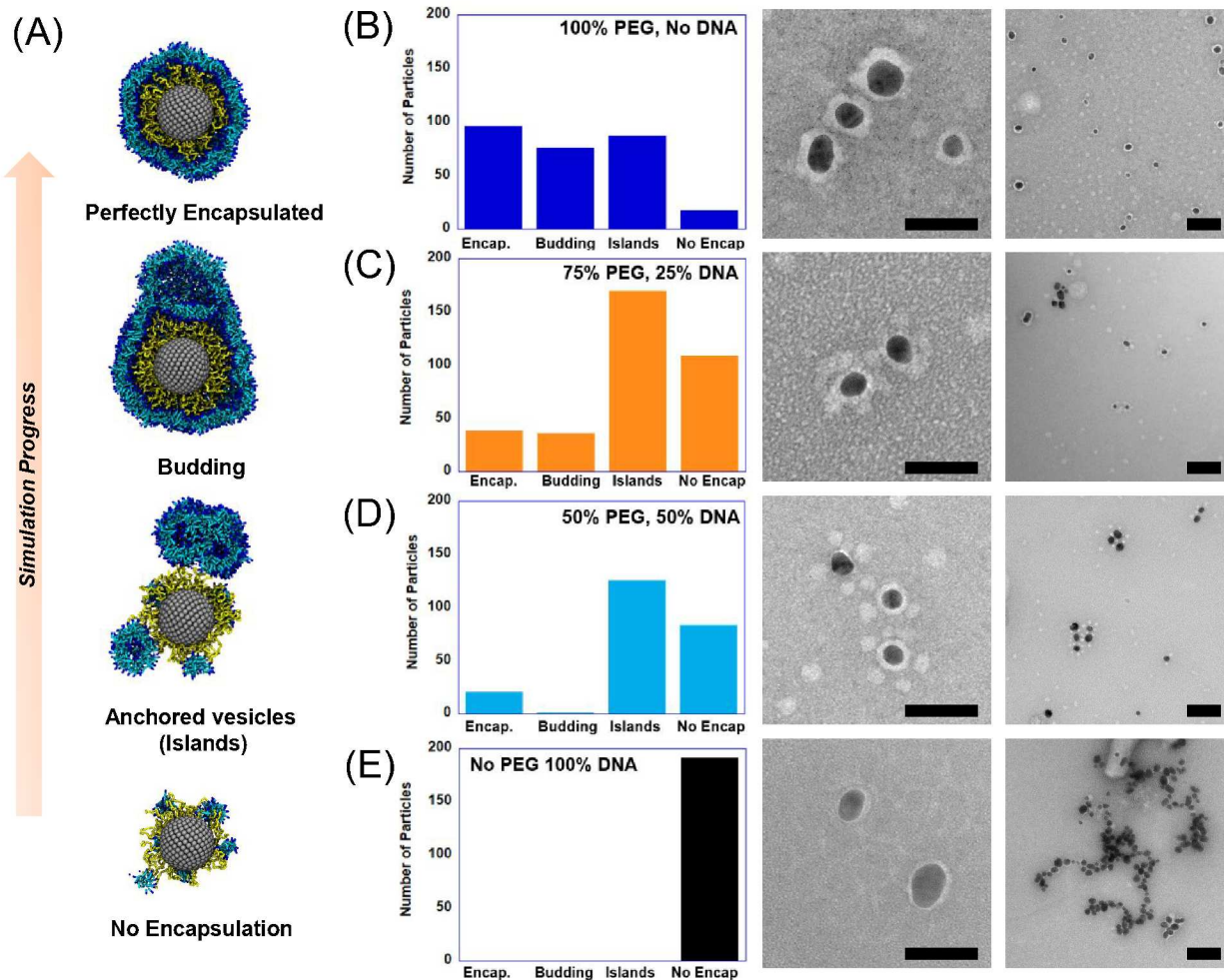
Figure 4. (A) Computed images of the major morphology categories observed through in silico experiments. (B-E) TEM and statistical characterization of 100%, 75%, 50%, 0% PEG-DSPE CPLS NPs. Scale bars are 50 nm for higher magnification, 100 nm for lower magnification. Samples are stained with 0.5% uranyl acetate. Statistical parameters are discussed in Supporting Information, Section 3
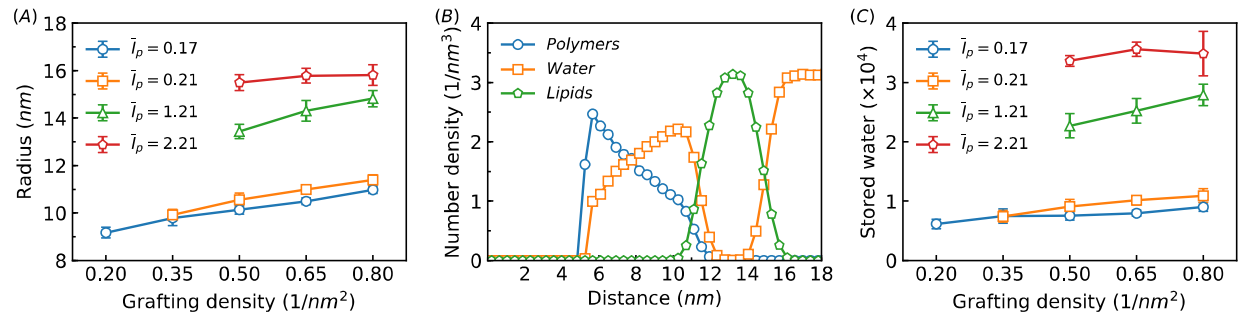
Figure 5. Properties of the perfectly encapsulated TMLs. (A) Radius of a perfectly encapsulated TML as a function of tethered polymer grafting density at different persistence lengths. (B) Radial bead number density of a perfectly encapsulated TML with $\bar{l}_p = 0.21$, $\sigma_g = 0.8 \, / \, nm^2$, $N_f = 5500$. (C) Number of stored water beads within the encapsulating lipid bilayer.
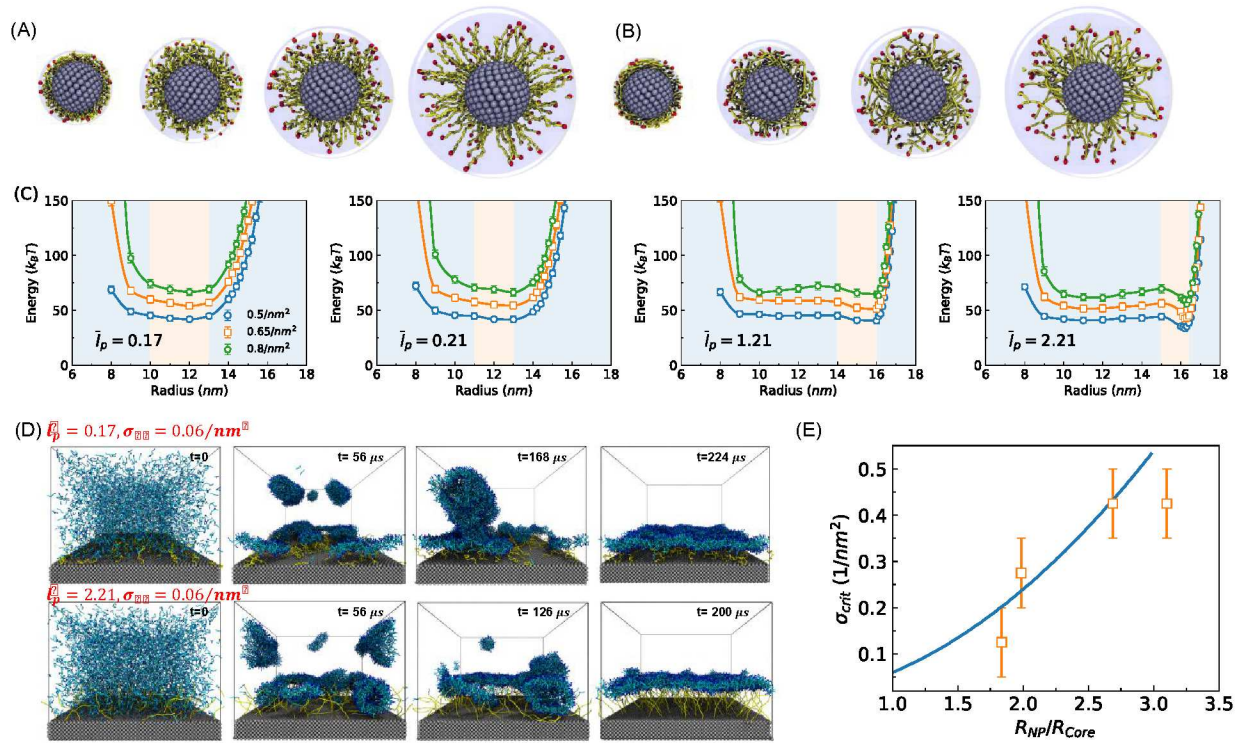
Figure 6. Estimation of required free lipid number and tethered polymer grafting density for perfectly encapsulated TMLs. (A-B) Schematic of indenter test for polymer tethered cores at the normalized persistence lengths of (A) $\overline{l_p} = 0.17$ and (B) $\overline{l_p} = 2.21$. The red beads are those polymer terminals that can freely translate on the indenter wall. The indenter wall will produce an outward repulsive force for the terminal beads, if their positions are inside the indenter wall. On the other hand, the indenter wall will produce an inward force for other polymer beads, if their positions are outside the indenter wall. (C) Tethered polymer free energy as a function of the indenter size at different tethered polymer persistence lengths. The optimal indenter size is marked in light red. (D) Self-assembly process of planar tethered lipid bilayers at different polymer persistence lengths. An intact membrane is formed at the grafting density of $\sigma_{pc} = 0.06 \, / \, nm^2$ for each case. (E) Comparison of the estimated critical grafting density obtained with Equation 2 (solid line) and those values in the phase diagram (scattered points).